https://doi.org/10.5194/egusphere-2026-1866
Preprint. Discussion started: 13 July 2026

A Fast Spectral Line-Ratio Algorithm for Mesospheric Airglow Rotational Temperature Retrieval and Validation

Shuqi Niu [1], Shengyang Gu[1,2], Haiyang Gao[3], Dini Gong[1], Yafei Wei[1], Yusong Qin[1]

[1] School of Earth and Space Science and Technology, Wuhan University, Wuhan 430072, China
[2]Wuhan Institute of Quantum Technology, Wuhan, 430072, China
[3]State Key Laboratory of Environment Characteristics and Effects for Near-space, Nanjing University of Information Science and Technology, Nanjing 210044, China

Correspondence to: Shengyang Gu (gushengyang@whu.edu.cn)

Abstract. Airglow rotational temperatures are effective tracers of variability in the mesopause region. To enable efficient processing of long-duration, high-temporal-resolution observations from the Mesospheric Airglow Spectrum Photometer (MASP), a Fast Airglow Spectral Line-Ratio algorithm (FASLR) is developed for rotational temperature retrieval. FASLR uses forward-modeled synthetic spectra to establish ratio–temperature relationships, derives independent temperature estimates from multiple line-intensity ratios, and combines them with weights based on the relative sensitivity of each ratio to instrumental perturbations. By avoiding computationally intensive multi-parameter iterative optimization, the algorithm substantially improves computational efficiency and remains robust to occasional anomalies in individual spectral lines. FASLR is validated using two nights of co-located MASP and sodium fluorescence Doppler lidar observations, showing good consistency with the corresponding lidar temperatures. The algorithm is then applied to six nights of dual-channel MASP observations of the O_2 (0–1) and OH (6–2) emissions and compared with independent temperatures from SABER, Aura/MLS, SD-WACCMX, and NRLMSIS 2.1. Overall, these comparisons indicate general consistency in the background temperature level, the relative offset between the O_2 and OH emission layers, and the range of nocturnal variability. Near representative emission-layer altitudes, the O_2 rotational temperatures reproduce the nocturnal background evolution reasonably well, whereas the OH temperatures show a more evident early-night high bias but better agreement during the latter half of the night. Case studies further demonstrate that the FASLR-derived temperatures are suitable for quantitative analyses of both longer-period nocturnal variability and shorter-period disturbances. On 2 February 2024, temperature and intensity perturbations in

https://doi.org/10.5194/egusphere-2026-1866
Preprint. Discussion started: 13 July 2026

the O_2 and OH layers exhibit a common dominant period band and stable phase relationships. On 7 February 2024, both layers show concurrent power enhancements within a similar period band, and simultaneous observations from the Mesospheric Airglow Wide-angle Imager (MAWI) independently support the identified disturbance. Overall, FASLR provides an efficient and robust approach for dual-channel airglow temperature retrieval and supports investigations of multi-scale wave processes in the mesopause region.

Keywords Temperature retrieval, Airglow Spectrum Photometer, Spectral line ratio, Dual-channel airglow observations, Data comparison, Gravity waves

1.Introduction

The mesosphere and lower thermosphere (MLT, ~50–120 km) lies between the lower atmosphere and the thermosphere–ionosphere system and forms a key transition region for vertical coupling across atmospheric layers. Within the MLT, the mesopause region is of particular importance. Its temperature is a key parameter for characterizing multiscale dynamical processes and associated energy transfer, and for assessing long-term changes in the upper atmosphere in a changing climate (Li et al., 2010; Wan and Xu, 2014; Yue et al., 2015; Chen et al., 2016; Yi et al., 2023). However, the thermal structure of the mesopause region exhibits pronounced spatiotemporal variability, and single-point observations are often insufficient to capture both its regional structure and temporal evolution. Coordinated multi-instrument observations and observational networks can provide continuous temporal coverage and spatial context, thereby placing important constraints on large-scale circulation, wave propagation, and interlayer coupling processes (Shepherd et al., 2020; Stober et al., 2021; Wang et al., 2022; Yang et al., 2024).

Among the available approaches, passive optical remote sensing is particularly well suited for temperature observations in the mesopause region. Nocturnal airglow emissions, such as O_2 and OH, contain rotational spectral features whose line intensities and intensity ratios can be used to retrieve rotational temperature (Sargoytchev et al., 2004; French et al., 2020; Wüst et al., 2023). Airglow spectrometers are relatively simple, operationally stable, and well suited for long-term continuous operation, and they have been deployed in observational networks to support regional-scale temperature intercomparisons and variability studies (Shepherd et al., 2002; Reisin et al., 2014; Xu et al., 2015). In China, temperature retrieval methods based on OH and

https://doi.org/10.5194/egusphere-2026-1866
Preprint. Discussion started: 13 July 2026

O_2 rotational spectra have also been explored (Xiong et al., 2012; Liu et al., 2015), further demonstrating the potential of this approach for broader deployment in observational networks. Continuous MLT airglow observations provide valuable information on temporal variability. Efficient and reliable data processing and temperature retrieval are therefore essential for fully exploiting these measurements, particularly in studies of short-term temperature variability, wave dynamics, and model evaluation.

To fully exploit continuous high-temporal-resolution airglow observations, temperature retrieval methods must be computationally efficient while maintaining accuracy and stability. Early approaches often relied on a limited number of rotational lines or line-intensity ratios to estimate temperature (Takeuchi and Misawa, 1979; Takeuchi et al., 1979). These methods are conceptually straightforward and require only limited spectral information, but they are sensitive to variations in signal-to-noise ratio (SNR), background contamination, and uncertainties in line-intensity parameters. Subsequently, multi-line approaches based on Boltzmann-plot regression of several rotational transitions were increasingly adopted for rotational temperature retrieval and provided greater robustness than single-line or line-pair methods (Sigernes et al., 2003; Mulligan et al., 2009). Advances in instrumentation and high-resolution spectroscopy, together with improved spectroscopic data for OH transitions, have further improved the accuracy and reliability of airglow temperature retrievals (Osterbrock et al., 1996; Brooke et al., 2016; Noll et al., 2023). However, the high cost of instrumentation and the complexity of the associated observational requirements continue to limit the broader use of these approaches in long-term and networked observations. More recently, optimal-estimation frameworks have also been explored in airglow remote sensing, allowing the incorporation of a priori constraints and a more rigorous characterization of posterior uncertainty (Sun et al., 2022). Although physically consistent, such approaches are typically more complex to implement and computationally more demanding than simpler line-ratio-based retrieval schemes.

A multi-parameter iterative inversion algorithm (MPII) was previously developed for the Mesospheric Airglow Spectrum Photometer (MASP) to jointly optimize multiple variable system parameters within a forward spectral model, thereby reducing systematic errors and improving retrieval accuracy. The validity of MPII has been demonstrated through coordinated observations with a sodium fluorescence Doppler lidar (Niu et al., 2024). However, because MPII requires repeated iterations

https://doi.org/10.5194/egusphere-2026-1866
Preprint. Discussion started: 13 July 2026

for each retrieval, its computational cost increases rapidly when applied to long-duration, high-temporal-resolution observations, thereby limiting its efficiency for processing dense time series.

Overall, despite the strengths of existing methods, efficient processing of continuous airglow observations with high temporal resolution remains difficult, particularly for long-duration datasets. In this study, a fast rotational-temperature retrieval algorithm based on airglow line-intensity ratios is developed to improve processing efficiency while maintaining retrieval accuracy. The algorithm establishes ratio–temperature relationships using a forward model and combines multiple ratio-based temperature estimates using sensitivity-based weights to reduce the influence of occasional anomalies in individual spectral lines. This method provides an efficient and stable framework for temperature retrieval from continuous MASP observations and supports analyses of atmospheric variability and wave processes.

2. Instrumentation and Datasets

2.1 Dual-channel MASP configuration

MASP is a zenith-viewing airglow spectrum photometer with a field of view of 12.9°. To enable alternating observations of two airglow bands without modifying the original single-channel optical layout, a filter wheel was added to the original system for sequential measurements of the O_2 (0–1) and OH (6–2) emissions. In this study, representative emission heights of 94 km for O_2 and 87 km for OH are adopted. The exposure times are 3 min for the O_2 channel and 2 min for the OH channel, resulting in an effective dual-channel sampling cadence of approximately 5.3 min. Both interference filters have an aperture of 50 mm. Their center wavelengths are 867.1 nm for O_2 and 837.17 nm for OH, with corresponding bandwidths of 0.24 nm and 0.26 nm. Further details of the optical design and the original single-channel MASP configuration can be found in Niu et al. (2024) and are not repeated here.

2.2 Observations and datasets

2.2.1 MASP dual-channel observations

https://doi.org/10.5194/egusphere-2026-1866
Preprint. Discussion started: 13 July 2026

As shown in Fig. 1, the dual-channel MASP was deployed at the Tulihe Meteorological Observatory, Hulunbuir, Inner Mongolia (50.5°N, 122.6°E), where continuous observations were obtained from 2 to 7 February 2024. About 10 h of valid data are typically available for each night after quality control, providing sufficient temporal coverage for the variability analyses presented in this study.

Figure 1: Photograph of the observation setup at Tulihe, together with representative MASP dual-channel airglow images in the O_2 (0–1) and OH (6–2) bands and a representative from MAWI.

2.2.2 Sodium fluorescence Doppler lidar data

Coordinated MASP and sodium fluorescence Doppler lidar observations previously obtained at the National Space Science Center, Chinese Academy of Sciences, in Huairou, Beijing (40°N, 116°E), are used to evaluate the accuracy of the FASLR temperature retrievals. The sodium fluorescence Doppler lidar provides temperature profiles over 75–105 km with a temporal resolution of 10 min and a vertical resolution of 1 km. Details of the coordinated campaign and the MASP–lidar temperature intercomparison can be found in Niu et al. (2024). In the present study, the lidar temperatures are used only as an independent reference for algorithm validation.

https://doi.org/10.5194/egusphere-2026-1866
Preprint. Discussion started: 13 July 2026

2.2.3 Auxiliary datasets

To further evaluate the reliability of the retrieved dual-channel temperatures, independent comparisons are conducted using satellite temperature profiles, reference temperatures from SD-WACCMX and NRLMSIS 2.1, and wide-field airglow imager data. All datasets are converted to China local time (LTC, UTC+8) to ensure a consistent time reference.

Satellite temperature profiles are obtained from SABER and Aura/MLS during 2–7 February 2024. For comparison with the MASP observations, only satellite overpasses occurring within the MASP observation intervals are used, although orbital constraints usually limit the number of samples to one or two per night. Overpasses within a ±20° latitude and ±20° longitude window centered on the observation site (50.5°N, 122.6°E) are selected. To approximate the airglow emission layers, the satellite profiles are vertically averaged using altitude-dependent weights over 85–89 km for OH and 92–96 km for O_2, yielding representative layer temperatures.

Reference temperatures from SD-WACCMX and NRLMSIS 2.1 are extracted near the observation site and vertically averaged using altitude-dependent weights over 85–90 km for OH and 92–96 km for O_2. T To characterize the nocturnal background state and low-frequency variability, the six-night temperature time series are aligned to a common LTC axis and averaged point by point to construct mean nocturnal temperature curves. These curves are then compared with the corresponding mean variations in the MASP observations.

In addition, data from the Mesospheric Airglow Wide-angle Imager (MAWI), acquired simultaneously with MASP, are used to examine transient disturbances (Fig. 1). The imager covers 750–850 nm, with an exposure time of 3 min, a cadence of 6.8 min, and a field of view of 120°. After standard image preprocessing (Huang et al., 2025), the resulting gravity-wave band structures are compared with transient features identified in the MASP wavelet analysis in terms of their occurrence time and morphology.

https://doi.org/10.5194/egusphere-2026-1866
Preprint. Discussion started: 13 July 2026

3. Fast Airglow Spectral Line-Ratio Algorithm（FASLR）

3.1 Physical basis

Under near-local thermodynamic equilibrium (LTE), the relative intensities of rotational lines within a given vibrational band vary systematically with rotational temperature and can therefore be used to retrieve rotational temperature (Mies, 1974). For OH airglow, the applicability and limitations of this approach, including possible non-LTE effects, have been discussed by Noll et al. (2016). For optically thin airglow emissions, the intensity of an individual rotational line depends primarily on the population of the corresponding upper rotational level, as well as on line-specific molecular parameters and the instrumental spectral response. Forming line-intensity ratios can reduce common instrumental effects, but cannot fully remove line-dependent instrumental responses or the unequal sensitivities of different ratios to instrumental-parameter variations. The resulting ratios therefore depend mainly on rotational temperature and known line-specific constants, but they retain different sensitivities to instrumental perturbations. For the O_2 (0–1) airglow emission, whose peak altitude is near 94 km, the lower rotational levels are commonly assumed to be close to LTE. The retrieved rotational temperature can therefore be treated as a reasonable approximation of the ambient kinetic temperature (Mies, 1974). Under this assumption, the rotational temperature derived from a selected line pair can be expressed as:

$$T_{n,m}=\frac{E_{v'}(J_m')\text{-}E_{v'}(J_n')}{k\,ln\left[\frac{I_n}{I_m}\frac{A\left(J_m',v'\rightarrow J_{m+1}'',v''\right)}{A\left(J_n',v'\rightarrow J_{n+1}'',v''\right)}\frac{2J_m'+1}{2J_n'+1}\right]},\tag{1}$$

where $T_{n,m}$ is the rotational temperature derived from lines n and m, I_n and I_m are the corresponding line intensities, J'_n *and* J'_m are the upper-state rotational quantum numbers, $E_{v'}(J')$ is the upper-level energy, and A denotes the Einstein A coefficient for the corresponding transition. Equation (1) is given here in its standard line-ratio form to illustrate the physical basis of rotational temperature retrieval.

Based on this principle, the Fast Airglow Spectral Line-Ratio Algorithm (FASLR) is developed for temperature retrieval in the mesopause region. Rather than determining temperature by iterative fitting of the full observed spectrum, FASLR uses selected rotational lines in the O_2 (0–1) band to construct line-intensity ratios and establishes the corresponding ratio–temperature

https://doi.org/10.5194/egusphere-2026-1866
Preprint. Discussion started: 13 July 2026

relationships from forward-modeled synthetic spectra over a prescribed temperature range, from which multiple ratio-based temperature estimates can be obtained from the observed spectrum.

3.2 Temperature retrieval

Figure 2 illustrates the construction of synthetic spectra and the fitted ratio–temperature relationships used for rotational temperature retrieval in the O_2 (0–1) band. As shown in Fig. 2a, synthetic concentric-ring images are generated over a prescribed temperature range using a previously developed MASP forward model. This forward model combines spectroscopic parameters from the HITRAN database with atmospheric radiative transfer and the O_2 channel instrumental response (Niu et al., 2024).

For each temperature, the forward-modeled image is converted into a spectrum by averaging the signal within concentric annuli. The annular mean values are then arranged along the radial coordinate to form a synthetic spectrum. Repeating this procedure over the prescribed temperature range yields a set of synthetic spectra corresponding to different rotational temperatures (Fig. 2b). Within the O_2 (0–1) band, the P1(1)–P1(4) lines are selected for temperature retrieval. Among them, P1(3) exhibits the weakest temperature dependence over the considered range and is therefore chosen as the reference line. Three line-intensity ratios, P1(1)/P1(3), P1(2)/P1(3), and P1(3)/P1(4), are then constructed and fitted as functions of temperature over 130–280 K (Fig. 2c). For a given input spectrum, the peak intensities of P1(1)–P1(4) are extracted to calculate the corresponding line-intensity ratios. Each ratio is then converted to a temperature using its fitted ratio–temperature relationship, yielding three ratio-based temperature estimates for the same spectrum. For idealized synthetic spectra generated by the forward model, these estimates are identical. In actual retrievals, however, differences may remain among them. The final rotational temperature is therefore obtained by combining these estimates using sensitivity-informed weighting.

https://doi.org/10.5194/egusphere-2026-1866
Preprint. Discussion started: 13 July 2026

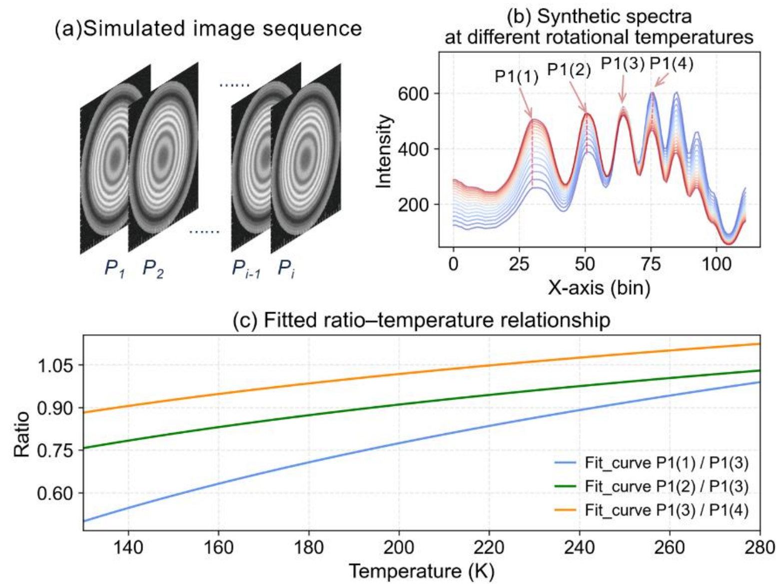

Figure 2: Construction of the synthetic spectra and fitted ratio–temperature relationships used for O_2 (0–1) rotational temperature retrieval. (a) Sequence of simulated concentric-ring images generated over the prescribed temperature range. (b) Synthetic spectra derived from the simulated images by annular averaging, with the P1(1)–P1(4) lines indicated. (c) Quadratic fits of the ratio–temperature relationships for P1(1)/P1(3), P1(2)/P1(3), and P1(3)/P1(4), from which ratio-based temperature estimates are obtained.

3.3 Sensitivity-based weighting

For each image, three ratio-based temperature estimates are obtained from the selected line-intensity ratios, namely P1(1)/P1(3), P1(2)/P1(3), and P1(3)/P1(4). If only a single ratio is used, the retrieval can be more strongly affected when one line is influenced by noise, background emission, or instrumental-parameter perturbations. The three estimates are therefore combined using a sensitivity-based weighting scheme.

The need for this weighting is illustrated in Fig. 3. In MPII, temperature retrieval relies on matching the full observed spectrum to simulated spectra and is therefore sensitive to changes in spectral shape. Figure 3a and 3b show that variations in filter temperature and optical-system focal length can substantially modify the spectral profile at a fixed rotational temperature. In FASLR, by contrast, temperature is inferred from line-intensity ratios rather than full-spectrum shape matching. As shown in Fig. 3c and d, the three selected ratios vary only weakly with these perturbations. The ratio-based approach therefore suppresses, but does not completely remove, the influence of instrumental-parameter variations. Moreover, Fig. 3e and 3f show that the residual sensitivity differs among ratios and varies with temperature. A simple arithmetic mean would therefore assign equal

https://doi.org/10.5194/egusphere-2026-1866
Preprint. Discussion started: 13 July 2026

importance to ratios with unequal stability. To reduce the influence of the more sensitive ratios, larger weights are assigned to ratios that are less sensitive to instrumental-parameter perturbations.

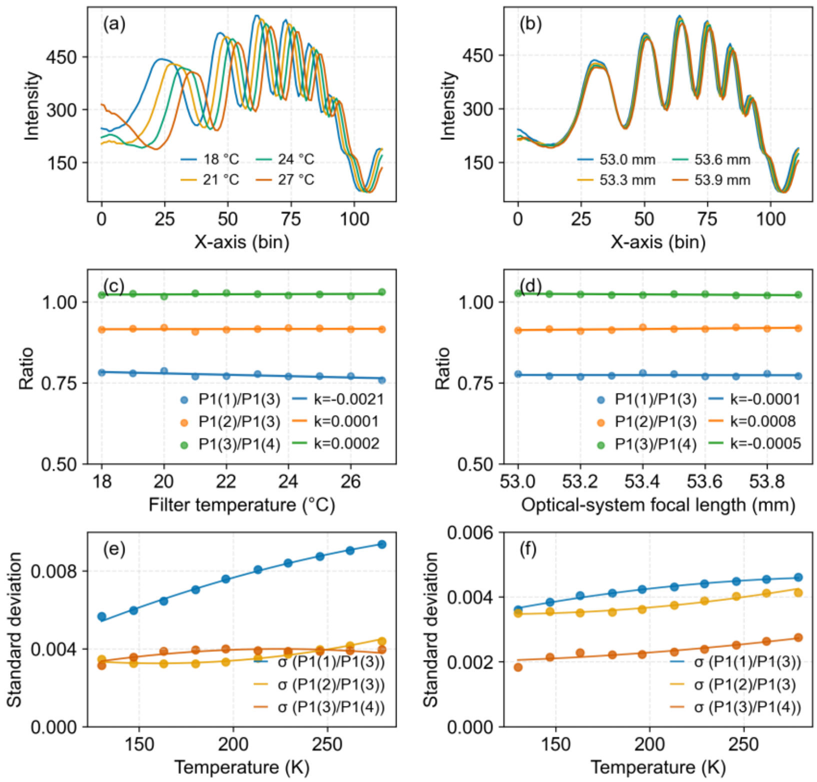

Figure 3: Sensitivity of the selected line-intensity ratios to instrumental-parameter perturbations. (a) Forward-modeled synthetic spectra at a fixed rotational temperature for different filter temperatures. (b) Same as (a) but for different optical-system focal lengths. (c) Dependence of the three selected line-intensity ratios on filter temperature at the same fixed rotational temperature, with linear fits shown for reference. (d) Same as (c) but for focal-length perturbations. (e) Temperature dependence of the standard deviation of each ratio under filter-temperature perturbations. (f) Same as (e) but for focal-length perturbations.

To quantify this sensitivity, single-parameter perturbation tests are performed using forward-modeled synthetic spectra. At a fixed rotational temperature T, the filter temperature T_f is varied over 18–27 °C while the focal length F is held fixed, and the F is varied over 53.0–53.9 mm while T_f is held fixed. For the i-th ratio R_i , the corresponding sensitivities are quantified by the standard deviations over the prescribed perturbation ranges:

$$\sigma_i^{(T_f)}(T)=Std\left[R_i\left(T;T_f\right)\right]\ ,\quad T_f\in[18\ ,27]°\mathrm{C}, \tag{2}$$

$$\sigma_i^{(F)}(T)=Std[R_i(T;F)]\ ,\quad F\in[53.0\ ,53.9]mm, \tag{3}$$

https://doi.org/10.5194/egusphere-2026-1866
Preprint. Discussion started: 13 July 2026

where i=1,2,3correspond to P1(1)/P1(3), P1(2)/P1(3), and P1(3)/P1(4), respectively, and Std is taken over the corresponding perturbation range. These quantities are evaluated over 130–280 K, and second-order polynomials are fitted to obtain continuous temperature-dependent sensitivity functions $\hat{\sigma}^{(T_f)}(T)$ and $\hat{\sigma}^{(F)}(T)$ as shown in Fig. 3e and 3f.

Because these sensitivities vary with temperature, the weights are evaluated adaptively for each observation rather than prescribed as constants. To ensure a consistent comparison among the three selected ratios, their sensitivities are evaluated at a common reference temperature T_{ref} representative of the current observation, rather than at three different ratio-specific temperatures. In this study, T_{ref} is taken as the median of the three ratio-based temperature estimates:

$$T_{ref}=\mathrm{median}(T_1, T_2, T_3). \tag{4}$$

The fitted sensitivity functions are then evaluated at T_{ref} to obtain the corresponding sensitivity measures for the current observation:

$$s_i^{(T_f)}(T)=\hat{\sigma}^{(T_f)}(T_{ref}), \qquad s_i^{(F)}(T)\hat{\sigma}^{(F)}(T_{ref}). \tag{5}$$

For each observation, these values are normalized to define the relative sensitivity coefficients:

$$p_i=\frac{s_i^{(T_f)}}{\sum_{j=1}^{3} s_j^{(T_f)}}, \qquad q_i=\frac{s_i^{(F)}}{\sum_{j=1}^{3} s_j^{(F)}}. \tag{6}$$

Assuming that the two effects are approximately independent, a combined sensitivity factor is defined as

$$r_i=1\text{-}(1\text{-}p_i)(1\text{-}q_i)\,, \quad r_i\in(0,1), \tag{7}$$

where a larger r_i indicates stronger overall sensitivity to instrumental-parameter perturbations. The preliminary weight is then defined inversely with respect to r_i :

$$w_i'=\frac{1}{(\varepsilon+r_i)}, \tag{8}$$

where $\varepsilon=10^{-6}$ is introduced to avoid division by zero. The normalized weight is:

$$w_i=\frac{w_i'}{\Sigma_{i=1}^{3} w_i'}\ . \tag{9}$$

The final temperature is computed as the weighted combination of the three ratio-based estimates:

$$T_{final}=\sum_{i=1}^{3} w_i T_i\,, \tag{10}$$

https://doi.org/10.5194/egusphere-2026-1866
Preprint. Discussion started: 13 July 2026

Accordingly, ratios that are less sensitive to instrumental-parameter perturbations receive larger weights and therefore contribute more strongly to the final temperature retrieval. Following the above calculations, the fitted weighting functions used to combine the three ratio-based temperature estimates are obtained, as shown in Fig. 4. The subsequent weighted retrieval is performed using these functions.

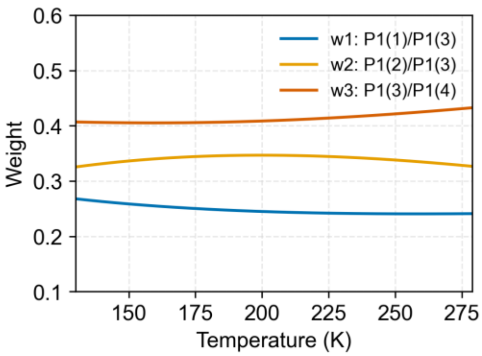

Figure 4: Fitted weighting functions used in the final weighted combination of the three ratio-based temperature estimates. The blue, yellow, and orange curves denote the weights assigned to the temperatures derived from P1(1)/P1(3), P1(2)/P1(3), and P1(3)/P1(4), respectively.

To estimate retrieval uncertainty, the statistical uncertainty of the annularly averaged spectrum was first evaluated at the bins corresponding to the selected line peaks and taken as the measurement uncertainty of each line intensity. For each line-intensity ratio, standard error propagation was used to derive the ratio uncertainty, which was then propagated through the fitted ratio-temperature relationship to estimate the uncertainty of the corresponding ratio-based temperature. The uncertainties of the individual ratio-based temperatures were finally combined using the same weights as in the temperature fusion to obtain the estimated uncertainty of each retrieval. The reported uncertainties mainly represent internal retrieval uncertainty derived from statistical error propagation and do not include additional external sources, such as emission-layer altitude variability or representativeness differences.

3.4 Practical application of FASLR and its advantages

3.4.1 Application and comparison with MPII

https://doi.org/10.5194/egusphere-2026-1866
Preprint. Discussion started: 13 July 2026

For retrieval from actual observations, the observed images are first preprocessed to obtain clear concentric-ring patterns with alternating bright and dark fringes, as shown in Fig. 5a. The preprocessing follows Niu et al. (2024), and the ring center is determined using the method of Wei et al. (2023). Using the identified ring center, each image is then converted into a radially averaged spectrum, as shown in Fig. 5b. To reduce the influence of greater random noise in the inner radial bins and stronger optical-aberration effects in the outer radial bins, the analysis is restricted to radial bin indices 20–80 in the 4 × 4 binned image, which encompass the P1(1)–P1(4) peaks shown in Fig. 5b. The peak intensities of these lines are then extracted to calculate the three line-intensity ratios used in the FASLR retrieval.

Figure 5c presents a representative case on 23 May 2023. The temperatures derived from the three individual line-intensity ratios differ substantially. The estimates from P1(2)/P1(3) remain systematically higher over most of the interval, whereas those from P1(3)/P1(4) are comparatively lower during the earlier part of the record and increase later. After sensitivity-based weighting is applied, the resulting FASLR temperatures lie between the individual estimates and exhibit a smoother temporal evolution. They are also broadly consistent with the main features of the MPII results, including the cooling near 23:30, the subsequent recovery after midnight, and the gradual warming later in the night. The estimated retrieval uncertainties mainly range from ±1.57 to ±2.68 K for FASLR and from ±0.50 to ±2.45 K for MPII. This comparison indicates that the sensitivity-based weighting moderates the influence of individual ratio-based estimates and provides a more stable combined temperature retrieval.

Figure 5d presents another case on 26 April 2023. Systematic differences among the three ratio-based temperature estimates are again evident. The estimates from P1(2)/P1(3) remain relatively high, whereas those from P1(3)/P1(4) are substantially lower over much of the interval. The weighted FASLR temperatures again fall between the individual estimates and remain broadly consistent with the trend of the MPII results, capturing the cooling before midnight and the subsequent warming after about 01:00. The FASLR temperatures are about 6–10 K higher than the MPII results. The estimated retrieval uncertainties mainly range from ±1.41 to ±2.15 K for FASLR and from ±1.96 to ±3.56 K for MPII. This case further indicates that the sensitivity-informed weighting yields a balanced combined retrieval while retaining the main temperature variability captured by MPII. The larger deviations near the end of the record are not emphasized here, because the measurements become less reliable as solar contamination increases.

https://doi.org/10.5194/egusphere-2026-1866
Preprint. Discussion started: 13 July 2026

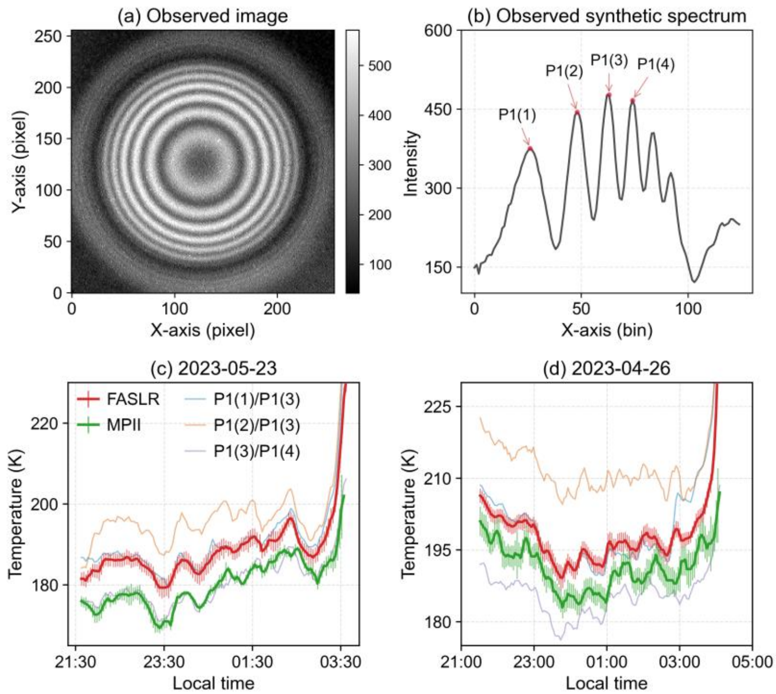

Figure 5: Practical application of FASLR to observed O_2 (0–1) spectra and comparison with MPII. (a) Preprocessed observed image showing clear concentric-ring fringes. (b) Radially averaged observed spectrum extracted from the image in panel (a), with the P1(1)–P1(4) peaks marked. Two representative cases showing the temperatures derived from the three selected line-intensity ratios, the final FASLR temperatures after sensitivity-based weighting, and the corresponding MPII results for 23 May 2023 (c) and 26 April 2023 (d), respectively. Error bars denote the estimated retrieval uncertainties of the FASLR and MPII temperatures.

3.4.2 Advantages of FASLR

MPII, previously developed for MASP, retrieves rotational temperature by iteratively matching the observed spectrum to forward-modeled spectra. In the MPII retrieval, multiple parameters, including rotational temperature, filter temperature, and optical-system focal length, are adjusted simultaneously until the spectral mismatch is minimized. Because the forward model must be evaluated repeatedly during each retrieval, MPII is time-consuming, particularly for continuous observations with large numbers of images.

In contrast, FASLR does not require iterative optimization of multiple parameters during retrieval. Instead, it establishes ratio–temperature relationships in advance from forward-modeled spectra, derives multiple ratio-based temperature estimates from the observed spectrum, and combines them using sensitivity-based weighting. It can also be extended to other airglow bands

https://doi.org/10.5194/egusphere-2026-1866
Preprint. Discussion started: 13 July 2026

in which temperature retrieval is based on the same line-ratio principle. For these bands, only the band-dependent spectroscopic inputs, channel-specific settings, and selected line ratios need to be adapted, while the forward-modeling procedure remains the same.

4. Comparative Validation of Retrieved Temperatures

4.1 Validation against sodium fluorescence Doppler lidar

Simultaneous MASP and sodium fluorescence Doppler lidar observations were previously conducted, and two nights of high-quality data were obtained. These two cases are used here to validate the temperatures retrieved by FASLR against the lidar observations. The observational setting and data processing are described in Sect. 2.2.2.

Figure 6 compares the FASLR and sodium fluorescence Doppler lidar temperatures for the two nights. On both nights, the FASLR temperatures are generally higher than the lidar temperatures, indicating a systematic mean temperature difference between the two datasets. This offset may reflect differences in measurement principle and atmospheric representativeness between the two instruments. Under such conditions, the correspondence in temporal evolution provides a more informative basis for assessing whether the FASLR retrievals reproduce the temperature variations observed by the lidar.

To facilitate comparison of the temperature variations, an additional analysis was performed by removing the mean bias between the two datasets over the common observing period. The bias was determined separately for each night and then subtracted from the FASLR temperature series. The resulting mean biases are 8.648 K on 23 May 2023 and 5.383 K on 26 April 2023. The bias-removed FASLR temperatures are shown by the dashed red curves in Fig. 6. This analysis was introduced only to highlight the similarity in temporal evolution and does not represent an absolute correction of the FASLR temperatures. As shown in Fig. 6a, after removal of the mean bias on 23 May 2023, the temporal evolution of the FASLR and lidar temperatures becomes more comparable. In particular, the major nocturnal variations, including the cooling before midnight and the subsequent warming later in the night, show better agreement between the two datasets. Some differences are still present, especially near the end of the record, when the data quality is likely reduced by the influence of the approaching sunrise and increasing daylight contamination. Nevertheless, after removal of the mean bias, the overall correspondence in

https://doi.org/10.5194/egusphere-2026-1866
Preprint. Discussion started: 13 July 2026

temperature evolution becomes more apparent. A similar result is obtained on 26 April 2023 (Fig. 6b). After removal of the mean bias, the agreement in temporal evolution becomes more evident, and the broad cooling before midnight together with the subsequent warming after midnight can be recognized more consistently in both datasets. Although differences remain in some parts of the record, the overall nocturnal evolution shows improved agreement.

Overall, although a mean temperature difference remains between the FASLR and lidar datasets, removal of the mean bias makes the agreement in their nighttime temperature evolution more evident, indicating that the FASLR retrievals can capture the main temporal variations observed by the lidar.

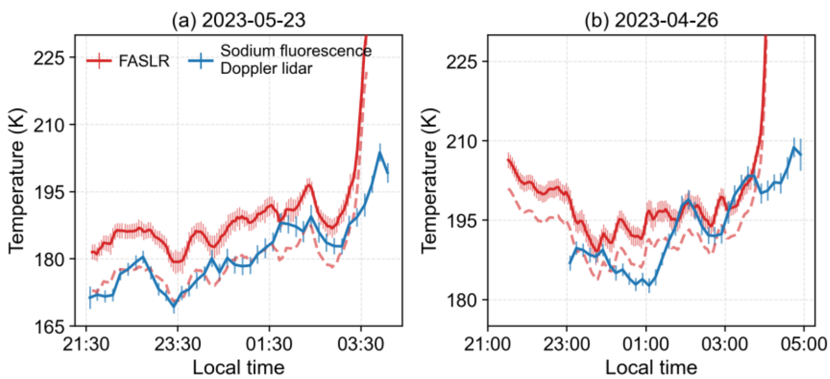

Figure 6: Comparison of the FASLR and sodium fluorescence Doppler lidar temperatures on (a) 23 May 2023 and (b) 26 April 2023. The solid red curves denote the original FASLR temperatures, the dashed red curves denote the FASLR temperatures after removal of the mean bias relative to the lidar over the common observing period, and the blue curves denote the lidar temperatures. Error bars indicate the corresponding retrieval uncertainties. The dashed curves are included only to facilitate comparison of the temporal evolution between the two datasets and do not represent an absolute correction of the FASLR temperatures.

4.2 Dual-channel observations and intercomparison with multi-source temperatures

4.2.1 Comparison with satellite observations

Figure 7 shows the nocturnal evolution of O_2 and OH rotational temperatures retrieved using FASLR, with valid measurements spanning approximately 19:00–05:30 local time (LT). For the OH (6–2) channel, temperatures were retrieved using the same forward-modeling and line-ratio-based procedure as that used for the O_2 (0–1) band, with only the band-specific spectroscopic inputs, channel settings, and selected line ratios adapted. Both channels show clear temporal variations over the night, with some similarities in their overall nocturnal evolution. The O_2 rotational temperatures are mainly distributed within 182–212 K,

https://doi.org/10.5194/egusphere-2026-1866
Preprint. Discussion started: 13 July 2026

with estimated retrieval uncertainties primarily in the range of ±1.7–3.2 K. The OH rotational temperatures mainly fall within 197–227 K, with estimated retrieval uncertainties primarily in the range of ±1.6–3.7 K, and are on average about 14 K higher than the O_2 temperatures. This behavior is consistent with previous airglow observations reported by Sargoytchev et al. (2004). As shown in Fig. 7, satellite data were further included as an independent consistency check. The collocated satellite temperatures exhibit noticeable scatter relative to the continuous ground-based retrievals. The available satellite comparisons show no obvious inconsistency in the overall temperature level, the relative offset between the OH and O_2 layers, or the magnitude of the nocturnal temperature variations. SABER temperatures are, on average, about 9.2 K higher than the retrieved values in the OH layer and about 9.7 K higher than those in the O_2 layer, consistent with earlier comparisons reported by López-González et al. (2007). By contrast, Aura/MLS temperatures are, on average, about 3 K lower than the retrieved values in the OH layer, but about 4.7 K higher than those in the O_2 layer.

Because satellite overpasses provide only limited temporal sampling and do not fully coincide with the continuous ground-based measurements in either time or location, a detailed comparison of nocturnal evolution is not feasible. In addition, differences in sampling geometry, field of view, and spatial resolution between satellite and ground-based observations, together with the limited vertical resolution and representativeness of satellite retrievals near the upper mesosphere, may also contribute to the remaining discrepancies. Nevertheless, the satellite comparisons do not indicate any obvious inconsistency in the retrieved temperature levels and provide useful external context for interpreting the observed nocturnal temperature variations.

https://doi.org/10.5194/egusphere-2026-1866
Preprint. Discussion started: 13 July 2026

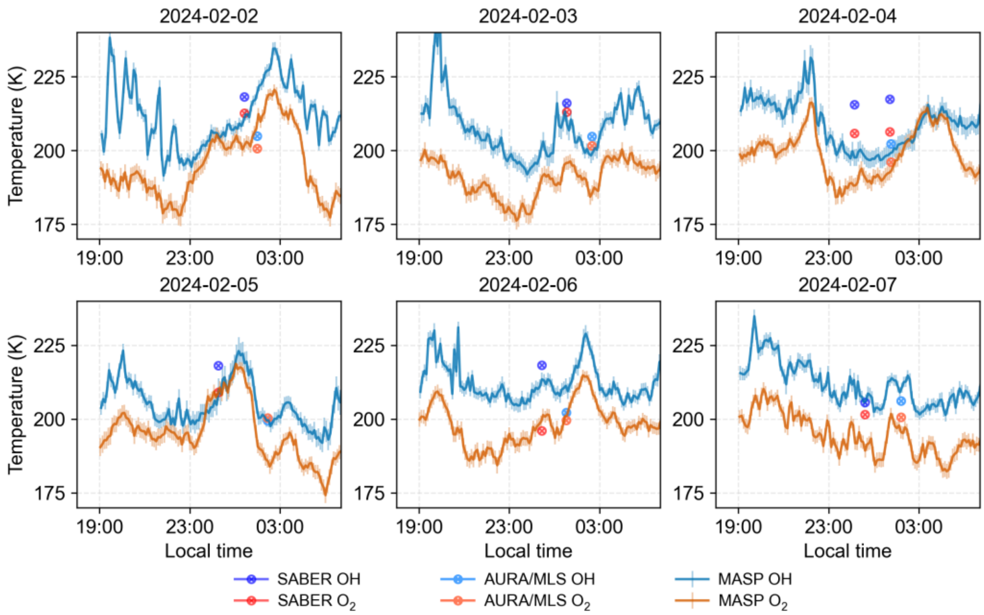

Figure 7: Rotational temperatures retrieved from MASP dual-channel observations on 2–7 February 2024 using the FASLR algorithm. The blue and orange curves represent the OH (6–2) and O_2 (0–1) rotational temperatures, respectively. Collocated satellite temperatures in the corresponding layers are indicated by colored circles: dark blue for SABER OH, dark red for SABER O_2, light blue for Aura/MLS OH, and light red for Aura/MLS O_2.

4.2.2 Comparison with SD-WACCMX and NRLMSIS 2.1

Figure 8 shows the composite nocturnal evolution of rotational temperature, obtained by aligning the six nights in local time and calculating the mean at each time stamp. The O_2 (0–1) rotational temperatures are mainly distributed within 185–200 K (Fig. 8a), whereas the OH (6–2) rotational temperatures are mainly distributed within 202–215 K, with a noticeable enhancement during the early part of the night (Fig. 8b). To further assess the accuracy of the retrieved temperatures, temperatures from the whole-atmosphere model SD-WACCMX and the empirical model NRLMSIS 2.1 are also included for comparison.

Because both models have coarser spatiotemporal resolution and different representativeness from the ground-based measurements, they cannot fully reproduce the short-term variability and local extrema captured by the observations. The comparison therefore focuses on the nighttime mean level and the slowly varying background component. For O_2 (0–1), the

https://doi.org/10.5194/egusphere-2026-1866
Preprint. Discussion started: 13 July 2026

nighttime mean temperature and low-frequency background from SD-WACCMX and NRLMSIS 2.1 are generally consistent with the retrieved temperatures, indicating that the FASLR results are physically reasonable at the background level. For OH, however, the composite temperatures are clearly higher than both model results during the early part of the night and gradually approach the model range later in the night. This indicates that the agreement for OH is more limited and is mainly evident during the middle and later parts of the night, rather than throughout the full nocturnal period.

The elevated OH temperatures during the early part of the night may reflect remaining representativeness differences between the actual OH emission layer and the fixed-range weighted model background, rather than a simple retrieval bias. Although the model temperatures were derived by weighted averaging over the altitude range corresponding to the OH emission region, the effective height and thickness of the OH layer may still vary with local time and atmospheric dynamics, even within a single night (Wüst et al., 2023). In addition, previous comparisons between ground-based OH temperatures and profile-based OH-equivalent temperatures have shown that variability in OH layer altitude and thickness can introduce biases when fixed or climatological weighting functions are used to derive OH-equivalent temperatures (Mulligan and Lowe, 2008). Short-term variability is also much weaker in the models, leading to differences in the detailed temporal evolution that are likely related to model resolution and sampling. Accordingly, the model–observation agreement is interpreted as support for the background-level reliability of the FASLR results, rather than as a direct validation of short-term perturbations. Overall, the composite comparison indicates that the FASLR retrievals capture a physically reasonable nocturnal background state, with stronger agreement with the models for O_2 (0–1) than for OH, especially during the early part of the night.

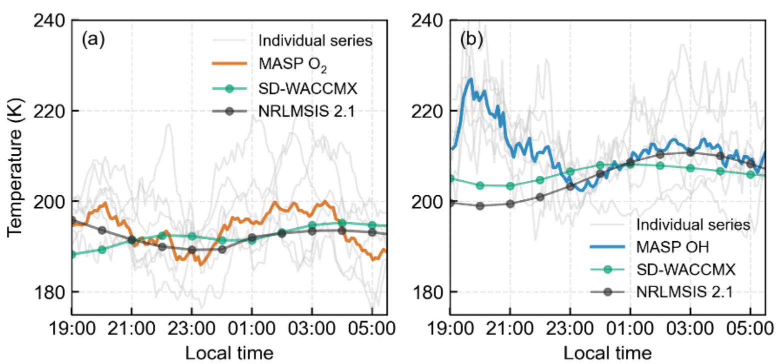

Figure 8: Composite nocturnal evolution of rotational temperatures from six observation nights and comparison with model results. (a) O_2 (0-1) rotational temperature. (b) OH (6–2) rotational temperature. The thick colored curves denote the composite mean of the

https://doi.org/10.5194/egusphere-2026-1866
Preprint. Discussion started: 13 July 2026

MASP-retrieved temperatures, while the green and black curves represent the SD-WACCMX and NRLMSIS 2.1 results, respectively. The faint gray curves indicate the individual nightly temperature series. The O_2 results are broadly consistent with the modeled background, whereas the OH temperatures are clearly elevated during the first part of the night, with model agreement improving during the latter part of the night.

5. Assessment of FASLR retrievals for wave diagnostics

To evaluate the capability of the FASLR temperature series for identifying wave signatures, the rotational temperature and emission intensity time series derived from the O_2 and OH channels were analyzed. Variability on different temporal scales was characterized using two complementary approaches, in which spectral analysis was employed to identify dominant periodic oscillations in the nighttime series, whereas wavelet analysis was applied to detect transient wave activity.

Two representative events from different observation nights are selected for illustration. The first case corresponds to 2 February 2024, when a stable dominant oscillation is observed throughout the night and analyzed using spectral methods. The second case corresponds to 7 February 2024, during which a transient enhancement of wave activity is detected and investigated using wavelet analysis.

5.1 Dominant oscillation on 2 February 2024

During the campaign, the effective observing duration for each night was ~10 h. The retrieved temperature time series therefore provides sufficient temporal coverage and resolution to support statistical analyses of whole-night variability. On this basis, consistency analyses of oscillations are performed using the dual-channel rotational temperature T(t) and emission intensity I(t).

The slowly varying nocturnal trend in the temperature and intensity series is removed by second-order polynomial detrending. The residual series are then normalized by the corresponding nightly mean values to obtain the relative perturbations, $\Delta T/T_0$ and $\Delta I/I_0$, where T_0 and I I_0 are the nightly mean temperature and intensity, respectively. These normalized perturbation series are subsequently analyzed using Lomb–Scargle analysis to identify the dominant long-period oscillation with periods longer than 6 h (Takahashi et al. 2011). A sinusoidal fit is then performed at the identified period to derive the amplitude, phase, and fit quality, which together characterize the primary features of the whole-night oscillation. Representative nights are identified

https://doi.org/10.5194/egusphere-2026-1866
Preprint. Discussion started: 13 July 2026

by requiring the dominant periods derived from temperature and intensity in both the O_2 and OH channels to agree within ±15%, and the corresponding sinusoidal fits to yield correlation coefficients r>0.7.

Among the six nights analyzed, only 2 February 2024 satisfied the above selection criteria and was therefore chosen for detailed analysis. Figure 9 illustrates the representative results for the night of 2 February 2024. Figure 9a and 9b present the O_2 and OH temperature series, respectively, while Figure 9c and d show the corresponding O_2 and OH emission-intensity series. In each panel, the upper part shows the raw time series together with the fitted second-order polynomial background, whereas the lower part shows the normalized residuals and the sinusoidal fit at the identified dominant period. The dominant periods derived from Fig.9 are 6.93, 6.90, 6.78, and 6.82 h, respectively, and the corresponding fit correlations all exceed 0.85, indicating a common long-period oscillation shared by temperature and intensity in both channels. The ~6.8–6.9 h signal is treated here as a common long-period component. Although a tidal contribution cannot be excluded, the present single-station analysis does not allow an unambiguous identification of its dynamical origin.

Given the common dominant period identified within each emission layer, the Krassovsky parameter, $\eta = |\eta| e^{-i\phi}$, is used to characterize the coupling between temperature and intensity perturbation. Here $|\eta|$ denotes the amplitude ratio of the relative intensity perturbation to the relative temperature perturbation, and ϕ represents the phase lag of intensity relative to temperature (Walterscheid et al., 1987; Taylor et al., 1991). In both the O_2 and OH layers, the temperature variation leads the intensity variation. In the O_2 layer, the temperature phase leads the intensity phase by about 15.4°, corresponding to approximately 17.5 min. In the OH layer, the phase lead is about 17.4°, equivalent to approximately 19.9 min. In addition, $|\eta|$ differs markedly between the two layers, with values of 5.85 for O_2 and 2.21 for OH, indicating a clear contrast in the amplitude response of intensity to temperature perturbations between the two emission layers.

Overall, these results show that, in addition to providing stable temperature retrievals, FASLR can support diagnostics of dominant periodicity, sinusoidal characteristics, and temperature–intensity coupling within each emission layer. This demonstrates its suitability for nocturnal airglow variability analysis.

https://doi.org/10.5194/egusphere-2026-1866
Preprint. Discussion started: 13 July 2026

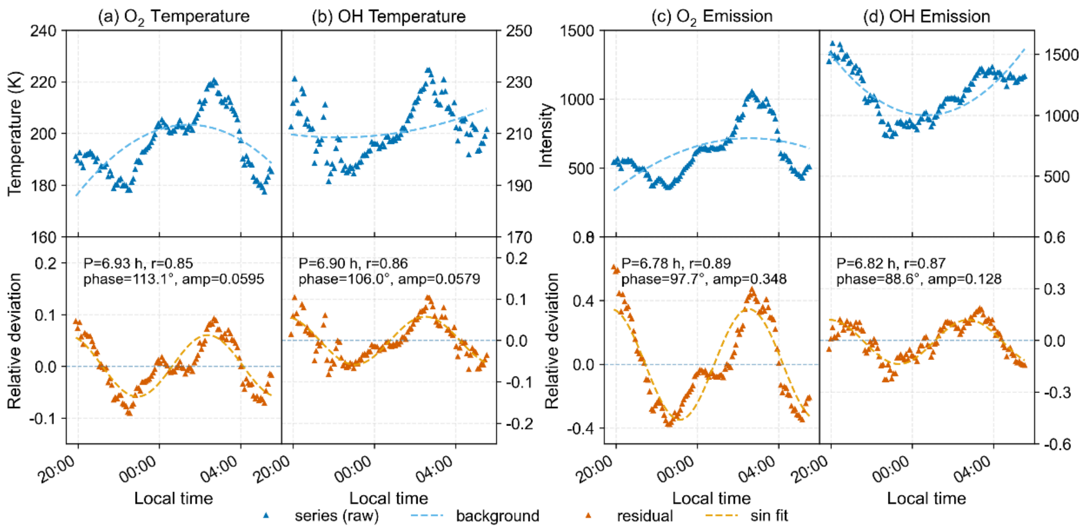

Figure 9: (a) O_2(0-1) temperature series; (b) OH (6-2) temperature series; (c) O_2 emission-intensity series; and (d) OH emission-intensity series. Blue triangles denote the raw series, and blue dashed lines denote the slowly varying background trend; orange triangles denote the normalized residuals, and orange dashed lines denote the sinusoidal fits. The labels in each panel indicate the dominant period (P), the correlation coefficient of the sinusoidal fit (r), the fitted phase (in degrees), and the fitted amplitude of the normalized residual series.

Table 1. Summary of dominant periods and sinusoidal fitting parameters for the series

Layer	Variable	Period(h)	Amplitude	phase (deg)	Correlation coefficient
O_2	(T'/T_0)	6.93	0.0595	113.1	0.8457
OH	(T'/T_0)	6.89	0.0579	106.0	0.8569
O_2	(I'/I_0)	6.78	0.3480	97.7	0.8936
OH	(I'/I_0)	6.82	0.1280	88.6	0.8713

5.2 Short-period disturbance on 7 February 2024

A continuous wavelet transform (CWT) was applied to the O_2 and OH rotational temperature and emission-intensity time series to identify short-period disturbances. A representative case occurred on 7 February 2024, when both channels exhibited enhanced short-period variability during the same nighttime interval. For the wavelet analysis, a moving-average method was

https://doi.org/10.5194/egusphere-2026-1866
Preprint. Discussion started: 13 July 2026

used to estimate the slowly varying background in the temperature and emission-intensity series, as shown in Fig. 10 a–d. The residual series obtained after background removal are presented in Fig. 10 e–h and were subsequently used for the continuous wavelet transform.

Figure 10 e–h show that, after removal of the slowly varying background, all four residual series oscillate around zero and exhibit clear quasi-periodic fluctuations. In both emission layers, the temperature residuals are relatively smooth and are reasonably well represented by the sinusoidal fits, whereas the intensity residuals show stronger intermittency and sharper local enhancements. This suggests that the short-period disturbance is present in both temperature and intensity, but with more pronounced non-stationarity in the emission-intensity series. Among the four series, the OH emission-intensity residual is the least regular and is associated with the most diffuse wavelet-power distribution, indicating that its short-period component is less well defined than in the other three series. Nevertheless, its main power enhancement still overlaps in both time and period with the other series, and is therefore interpreted as a weaker but still consistent response to the same short-period disturbance. The wavelet power spectra in Fig. 10 i–l show enhanced short-period power on 7 February 2024. In Fig. 10 i–k, the dominant power enhancement is concentrated mainly within a common period range of about 1.5–2.2 h and occurs primarily during about 00:00–03:00 LT, although the exact peak period varies somewhat among variables. Compared with the other three series, the OH emission-intensity spectrum is more diffuse, suggesting that its short-period response is modulated by additional variability rather than dominated by a single narrow-band component. Nevertheless, its enhanced power still overlaps partially with the other series in time–period space, supporting the presence of a common short-period disturbance in the two emission layers.

https://doi.org/10.5194/egusphere-2026-1866
Preprint. Discussion started: 13 July 2026

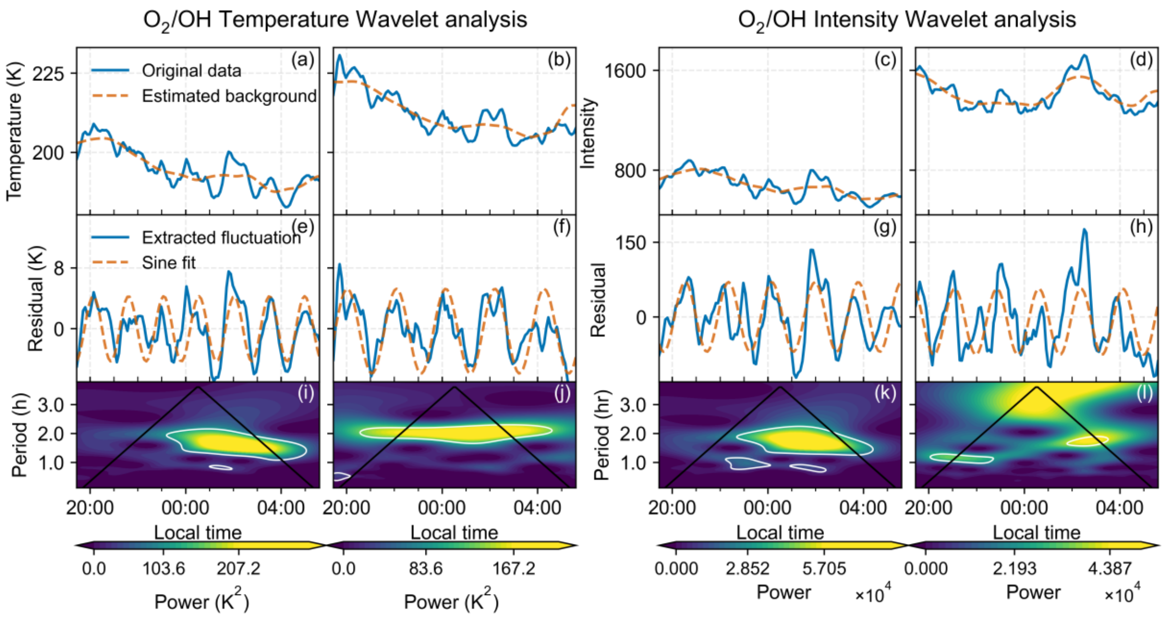

Figure 10: (a), (b) Original O_2 and OH temperature series with the estimated slowly varying background. (c), (d) Original O_2 and OH emission-intensity series with the estimated slowly varying background. (e), (f) Residual temperature series after background removal, together with sinusoidal fits. (g), (h) Residual emission-intensity series after background removal, together with sinusoidal fits. (i)- (l) Continuous wavelet power spectra corresponding to panels (e)-(h). The black curves denote the cone of influence, and the white contours indicate the 95% significance level.

To provide additional context for the short-period disturbance identified from MASP, simultaneous observations from MAWI were also examined. A zenith-centered region with a radius of 8° was selected from the MAWI images, and the median intensity within this region was used to construct a regional intensity time series. As shown in Fig. 11a and 11b, the slowly varying background was estimated using a moving-average method and removed to obtain the fluctuation series. The wavelet power spectrum in Fig. 11c shows enhanced short-period power mainly near 1.4–1.6 h during about 00:00–03:00 LT, overlapping the time interval of the MASP disturbance and partially overlapping its period range. Meanwhile, the corresponding imager frames in Fig. 11d display continuous band-like structures characteristic of gravity-wave activity. These independent observations therefore provide supportive evidence that a short-period gravity-wave disturbance was present during the interval identified from the MASP data.

https://doi.org/10.5194/egusphere-2026-1866
Preprint. Discussion started: 13 July 2026

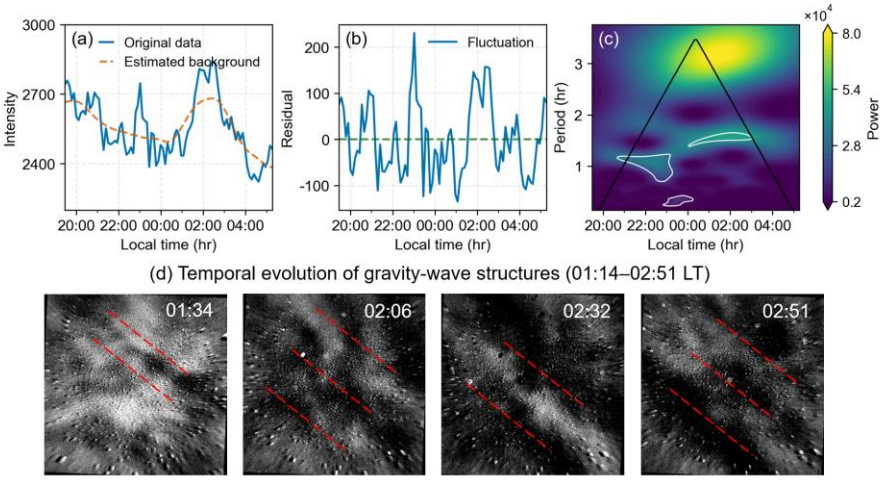

Figure 11: (a) Zenith-region intensity series and estimated background. (b) Background-removed fluctuation series. (c) Wavelet power spectrum of the fluctuation series (d) Representative imager frames during 01:14–02:51 LT, showing band-like gravity-wave structures. These observations provide independent support for the existence of a short-period gravity-wave disturbance during the MASP event interval.

6. Discussion Conclusions

FASLR was developed as an efficient and accurate method for retrieving airglow rotational temperatures from MASP observations in the mesopause region. By establishing ratio–temperature relationships from forward-modeled synthetic spectra and combining multiple ratio-based temperature estimates with sensitivity- based weights, FASLR avoids the multi-parameter iterative optimization required by MPII. As a result, it substantially improves computational efficiency while reducing sensitivity to occasional anomalies in individual spectral lines and retaining retrieval accuracy.

Validation against two nights of simultaneous MASP and sodium fluorescence Doppler lidar observations shows that the FASLR temperatures are consistent with the corresponding lidar measurements. FASLR was also applied to dual-channel rotational temperature retrievals for the O_2 (0–1) and OH (6–2) emissions. Comparisons with collocated temperatures from SABER and Aura/MLS indicate overall consistency in the background temperature level, the relative offset between the OH and O_2 layers, and the range of nocturnal variability. Given differences in sampling and representativeness, the interpretation focuses on these broader features. In comparison with SD-WACCMX and NRLMSIS 2.1 at the corresponding representative emission-layer altitudes, the O_2 rotational temperatures reproduce the nocturnal background evolution and temperature levels

https://doi.org/10.5194/egusphere-2026-1866
Preprint. Discussion started: 13 July 2026

reasonably well. By contrast, the OH rotational temperatures show a pronounced early-night high bias, although this discrepancy decreases as the night progresses and agreement with the model temperatures improves during the latter half of the night. This difference may be related to emission-layer altitude variability and to representativeness differences between ground-based observations and model fields.

Two representative cases further demonstrate that FASLR temperatures support quantitative analysis of variability on different temporal scales. On 2 February 2024, temperature and intensity perturbations in the O_2 and OH emission layers share a common dominant period band and stable phase relationships. These features support standard airglow wave diagnostics, including estimation of the Krassovsky parameter. On 7 February 2024, both emission layers exhibit concurrent power enhancements within similar period bands over the same interval, while simultaneous MAWI images reveal coherent banded structures. Together, these results demonstrate that FASLR temperatures are suitable for quantitative analysis of both longer-period nocturnal variability and shorter-period disturbances, supporting investigations of multi-scale wave processes in the mesopause region. Further efforts may also explore the development and validation of a framework for retrieving two-dimensional temperature-perturbation fields by combining FASLR temperatures with wave-structure information from MAWI image sequences.

Data availability

The datasets supporting this study are archived in Zenodo at https://doi.org/10.5281/zenodo.19363272. The deposited materials include the raw dual-channel MASP observations collected during the six nights from 2 to 7 February 2024; the processed temperature comparison data for 26 April 2023 and 23 May 2023, including the FASLR and MPII temperature series and the processed sodium fluorescence Doppler lidar temperature products used in the manuscript; and the representative MAWI image subset directly used in the gravity-wave event analysis presented in this study. The lidar data archived in the repository correspond to the processed temperature products used in this work rather than the original raw measurements. The SD-WACCMX data used in this study were generated by our group using the WACCM-X model in the specified-dynamics configuration and are available from the corresponding author upon reasonable request. Third-party datasets and model resources used in this work are available from their official sources. TIMED/SABER data were obtained from the SABER

https://doi.org/10.5194/egusphere-2026-1866
Preprint. Discussion started: 13 July 2026

Data Services portal. Aura/MLS data were obtained from the official Aura MLS data portal. The NRLMSIS 2.1 model is available through the NASA CCMC access pages. These third-party datasets and model resources are cited accordingly in the manuscript.

Code availability

The code used in this study is currently not publicly archived. The main routines for spectral processing and rotational temperature retrieval are available from the corresponding author upon reasonable request.

Author contributions

Conceptualization: Shuqi Niu

Formal analysis: Shengyang Gu, Shuqi Niu

Methodology: Shengyang Gu, Shuqi Niu, Haiyang Gao

Resources: Dini Gong, Yafei Wei, Yusong Qin

Validation: Shuqi Niu

Visualization: Shuqi Niu

Writing-original draft: Shuqi Niu

Writing-review & editing: Shengyang Gu

Competing interests

The authors declare that they have no conflict of interest.

https://doi.org/10.5194/egusphere-2026-1866
Preprint. Discussion started: 13 July 2026

Acknowledgements

This work was supported by the National Natural Science Foundation of China (Grant No. 42374223), the Natural Science Foundation of Wuhan (Grant 2025041001010362), the Fundamental Research Funds for the Central Universities (242025kf0035, 2042025gf0003).

References

Brooke, J. S. A., Bernath, P. F., Western, C. M., Sneden, C., Afşar, M., Li, G., and Gordon, I. E.: Line strengths of rovibrational and rotational transitions in the $X^2\Pi$ ground state of OH, J. Quant. Spectrosc. Ra., 168, 142–157, https://doi.org/10.1016/j.jqsrt.2015.07.021, 2016.

Chen, Z., Xu, J., Hu, X., Chen, H., Chen, W., Wei, K., Bian, J., Tian, W., Zhang, S., Ren, R., and Dou, X.: Advances in the researches of the middle and upper atmosphere in China in 2014–2016, Chin. J. Space Sci., 36, 738–752, https://doi.org/10.11728/cjss2016.05.738, 2016.

French, W. J. R., Mulligan, F. J., and Klekociuk, A. R.: Analysis of 24 years of mesopause region OH rotational temperature observations at Davis, Antarctica – Part 1: long-term trends, Atmos. Chem. Phys., 20, 6379–6394, https://doi.org/10.5194/acp-20-6379-2020, 2020.

Shepherd, M. G., Meek, C. E., Hocking, W. K., Hall, C. M., Partamies, N., Sigernes, F., Manson, A. H., and Ward, W. E.: Multi-instrument study of the mesosphere-lower thermosphere dynamics at 80°N during the major SSW in January 2019, J. Atmos. Sol.-Terr. Phys., 210, 105427, https://doi.org/10.1016/j.jastp.2020.105427, 2020.

Stober, G., Kozlovsky, A., Liu, A., Qiao, Z., Tsutsumi, M., Hall, C., Nozawa, S., Lester, M., Belova, E., Kero, J., Espy, P. J., Hibbins, R. E., and Mitchell, N.: Atmospheric tomography using the Nordic Meteor Radar Cluster and Chilean Observation Network De Meteor Radars: network details and 3D-Var retrieval, Atmos. Meas. Tech., 14, 6509–6532, https://doi.org/10.5194/amt-14-6509-2021, 2021.

Yang, Y., Li, F., Cheng, X., Yang, G., Lyu, D., Lin, X., Liu, L., Fang, X., Zheng, J., Du, L., Wang, W., Ren, L., Wang, J., Liang, J., Ji, K., Xu, L., Chen, Z., Ji, K., Zheng, H., Wang, X., Wang, Y., Jiao, J., Wang, X., Xue, X., Xia, Y., Li, Y., Lin, Z.,

https://doi.org/10.5194/egusphere-2026-1866
Preprint. Discussion started: 13 July 2026

Chen, L., Chen, Z., Xu, J., Li, G., Hu, L., and Gong, S.: Lidar Network for Temperature and Wind Measurements in the Mesosphere and Lower Thermosphere Region, Space Weather, 22, e2024SW003981, https://doi.org/10.1029/2024SW003981, 2024.

Huang, H., Gu, S.-Y., Qin, Y., Li, G., Yang, Z., Wei, Y., Gong, D., and Niu, S.: Statistical analysis of gravity waves in the mesopause region based on OI 557.7 nm airglow observation over Mohe, China, J. Geophys. Res.-Space, 130, e2025JA033917, https://doi.org/10.1029/2025JA033917, 2025.

Li, T., Leblanc, T., McDermid, I. S., Wu, D. L., Dou, X. K., and Wang, S.: Seasonal and interannual variability of gravity wave activity revealed by long-term lidar observations over Mauna Loa Observatory, Hawaii, J. Geophys. Res.-Atmos., 115, D13103, https://doi.org/10.1029/2009JD013586, 2010.

Liu, W., Xu, J., Smith, A. K., and Yuan, W.: Comparison of rotational temperature derived from ground-based OH airglow observations with TIMED/SABER to evaluate the Einstein coefficients, J. Geophys. Res.-Space, 120, 10069–10082, https://doi.org/10.1002/2015JA021886, 2015.

López-González, M.J., García-Comas, M., Rodríguez, E., López-Puertas, M., Shepherd, M.G., Shepherd, G.G., Sargoytchev, S., Aushev, V.M., Smith, S.M., Mlynczak, M.G., Russell, J.M., Brown, S., Cho, Y., and Wiens, R.H.: Ground-based mesospheric temperatures at mid-latitude derived from O_2 and OH airglow SATI data: Comparison with SABER measurements, J. Atmos. Sol.-Terr. Phy., 69, 2379–2390, https://doi.org/10.1016/j.jastp.2007.07.004, 2007.

Mies, F. H.: Calculated vibrational transition probabilities of OH($X^2\Pi$), J. Mol. Spectrosc., 53, 150–188, https://doi.org/10.1016/0022-2852(74)90125-8, 1974.

Mulligan, F. J. and Lowe, R. P.: OH-equivalent temperatures derived from ACE-FTS and SABER temperature profiles – a comparison with OH*(3–1) temperatures from Maynooth (53.2° N, 6.4° W), Ann. Geophys., 26, 795–811, https://doi.org/10.5194/angeo-26-795-2008, 2008.

Mulligan, F. J., Dyrland, M. E., Sigernes, F., and Deehr, C. S.: Inferring hydroxyl layer peak heights from ground-based measurements of OH (6–2) band integrated emission rate at Longyearbyen (78° N, 16° E), Ann. Geophys., 27, 4197–4205, https://doi.org/10.5194/angeo-27-4197-2009, 2009.

https://doi.org/10.5194/egusphere-2026-1866
Preprint. Discussion started: 13 July 2026

Niu, S., Gao, H., Yan, Z., Ren, K., Kou, L., Jiang, B., and Bu, L.: High-precision temperature retrieval algorithm and verification for mesospheric airglow spectrum photometer, Sci. China Earth Sci., 67, 1639–1651, https://doi.org/10.1007/s11430-023-1298-y, 2024.

Noll, S., Kausch, W., Kimeswenger, S., Unterguggenberger, S., and Jones, A. M.: Comparison of VLT/X-shooter OH and O_2 rotational temperatures with consideration of TIMED/SABER emission and temperature profiles, Atmos. Chem. Phys., 16, 5021–5042, https://doi.org/10.5194/acp-16-5021-2016, 2016.

Noll, S., Schmidt, C., Kausch, W., Bittner, M., and Kimeswenger, S.: Climatologies of Various OH Lines From About 90,000 X-Shooter Spectra, J. Geophys. Res.-Atmos., 128, e2022JD038275, https://doi.org/10.1029/2022JD038275, 2023.

Osterbrock, D. E., Fulbright, J. P., Martel, A. R., Keane, M. J., Trager, S. C., and Basri, G.: Night-sky high-resolution spectral atlas of OH and O_2 emission lines for echelle spectrograph wavelength calibration, Publ. Astron. Soc. Pac., 108, 277–308, https://doi.org/10.1086/133722, 1996.

Reisin, E. R., Scheer, J., Dyrland, M. E., Sigernes, F., Deehr, C. S., Schmidt, C., Höppner, K., Bittner, M., Ammosov, P. P., Gavrilyeva, G. A., Stegman, J., Perminov, V. I., Semenov, A. I., Knieling, P., Koppmann, R., Shiokawa, K., Lowe, R. P., López-González, M. J., Rodríguez, E., Zhao, Y., Taylor, M. J., Buriti, R. A., Espy, P. J., French, W. J. R., Eichmann, K.-U., Burrows, J. P., and von Savigny, C.: Traveling planetary wave activity from mesopause region airglow temperatures determined by the Network for the Detection of Mesospheric Change (NDMC), J. Atmos. Sol.-Terr. Phy., 119, 71–82, https://doi.org/10.1016/j.jastp.2014.07.002, 2014.

Sargoytchev, S. I., Brown, S., Solheim, B. H., Cho, Y.-M., Shepherd, G. G., and López-González, M. J.: Spectral airglow temperature imager (SATI): a ground-based instrument for the monitoring of mesosphere temperature, Appl. Opt., 43, 5712–5721, https://doi.org/10.1364/AO.43.005712, 2004.

Shepherd, G. G., Hagan, M., and Portnyagin, Y.: PSMOS 2000 workshop – planetary scale mesopause observing system, J. Atmos. Sol.-Terr. Phy., 64, 873–874, https://doi.org/10.1016/S1364-6826(02)00038-X, 2002.

Sigernes, F., Shumilov, N., Deehr, C. S., Nielsen, K. P., Svenøe, T., and Havnes, O.: Hydroxyl rotational temperature record from the auroral station in Adventdalen, Svalbard (78° N, 15° E), J. Geophys. Res.-Space, 108, 1342, https://doi.org/10.1029/2001JA009023, 2003.

Sun, K., Yousefi, M., Chan Miller, C., Chance, K., González Abad, G., Gordon, I. E., Liu, X., O'Sullivan, E., Sioris, C. E., and Wofsy, S. C.: An optimal estimation-based retrieval of upper atmospheric oxygen airglow and temperature from SCIAMACHY limb observations, Atmos. Meas. Tech., 15, 3721–3745, https://doi.org/10.5194/amt-15-3721-2022, 2022.

Takahashi, H., Onohara, A., Shiokawa, K., Vargas, F., and Gobbi, D.: Atmospheric wave induced O_2 and OH airglow intensity variations: effect of vertical wavelength and damping, Ann. Geophys., 29, 631–637, https://doi.org/10.5194/angeo-29-631-2011, 2011.

Takeuchi, I. and Misawa, K.: Successive approximation for determining the hydroxyl rotational temperature, Appl. Opt., 18, 3805–3809, https://doi.org/10.1364/AO.18.003805, 1979.

Takeuchi, I., Misawa, K., Kato, Y., and Aoyama, I.: Rotational temperatures and intensities of OH(6–2) and OH(8–3) bands in the night airglow, J. Atmos. Terr. Phys., 41, 387–395, https://doi.org/10.1016/0021-9169(79)90035-7, 1979.

Taylor, M. J., Espy, P. J., Baker, D. J., Sica, R. J., Neal, P. C., and Pendleton Jr., W. R.: Simultaneous intensity, temperature and imaging measurements of short period wave structure in the OH nightglow emission, Planet. Space Sci., 39, 1171–1188, https://doi.org/10.1016/0032-0633(91)90169-B, 1991.

Walterscheid, R. L., Schubert, G., and Straus, J. M.: A dynamical-chemical model of wave-driven fluctuations in the OH nightglow, J. Geophys. Res., 92, 1241–1254, https://doi.org/10.1029/JA092iA02p01241, 1987.

Wan, W. and Xu, J.: Recent investigation on the coupling between the ionosphere and upper atmosphere, Sci. China Earth Sci., 57, 1995–2012, https://doi.org/10.1007/s11430-014-4923-3, 2014.

Wang, J., Yi, W., Wu, J., Chen, T., Xue, X., Zeng, J., Vincent, R. A., Reid, I. M., Batista, P. P., Buriti, R. A., Tsuda, T., Mitchell, N. J., and Dou, X.: Coordinated observations of migrating tides by multiple meteor radars in the equatorial mesosphere and lower thermosphere, J. Geophys. Res.-Space, 127, e2022JA030678, https://doi.org/10.1029/2022JA030678, 2022.

Wei, Y., Gu, S.-Y., Yang, Z., Huang, C., Li, N., Hu, G., and Dou, X.: Inversion of wind and temperature from low SNR FPI interferograms, Remote Sens., 15, 1934, https://doi.org/10.3390/rs15071934, 2023.

https://doi.org/10.5194/egusphere-2026-1866
Preprint. Discussion started: 13 July 2026

Wüst, S., Bittner, M., Espy, P. J., French, W. J. R., and Mulligan, F. J.: Hydroxyl airglow observations for investigating atmospheric dynamics: results and challenges, Atmos. Chem. Phys., 23, 1599–1618, https://doi.org/10.5194/acp-23-1599-2023, 2023.

Xiong, J., Wan, W. X., Ning, B., Liu, L., Wu, B., Hu, L., and Xu, T.: Seasonal variations of night mesopause temperature in Beijing observed by SATI4, Sci. China Technol. Sci., 55, 1295–1301, https://doi.org/10.1007/s11431-012-4779-8, 2012.

Xu, J., Li, Q., Yue, J., Hoffmann, L., Straka III, W. C., Wang, C., Liu, M., Yuan, W., Han, S., Miller, S. D., Sun, L., Liu, X., Liu, W., Yang, J., and Ning, B.: Concentric gravity waves over northern China observed by an airglow imager network and satellites, J. Geophys. Res.-Atmos., 120, 11058–11078, https://doi.org/10.1002/2015JD023786, 2015.

Yi, W., Xue, X., Lu, M., Zeng, J., Ye, H., Wu, J., Wang, C., and Chen, T..: Mesopause temperatures and relative densities at midlatitudes observed by the Mengcheng meteor radar, Earth Planet. Phys., 7, 665–674, https://doi.org/10.26464/epp2023083, 2023.

Yue, J., Russell III, J., Jian, Y., Rezac, L., Garcia, R, López-Puertas, M., and Mlynczak, M. G.: Increasing carbon dioxide concentration in the upper atmosphere observed by SABER, Geophys. Res. Lett., 42, 7194–7199, https://doi.org/10.1002/2015GL064696, 2015.